



X-Ray Diffraction of Solid Tin to 1.2 TPa

A. Lazicki,¹ J. R. Rygg,¹ F. Coppari,¹ R. Smith,¹ D. Fratanduono,¹ R. G. Kraus,¹
G. W. Collins,¹ R. Briggs,² D. G. Braun,¹ D. C. Swift,¹ and J. H. Eggert¹

¹Lawrence Livermore National Laboratory, 7000 East Avenue, Livermore, California 94550, USA

²The University of Edinburgh, Mayfield Road, Edinburgh EH9 3JZ, United Kingdom

(Received 30 April 2015; published 12 August 2015)

We report direct *in situ* measurements of the crystal structure of tin between 0.12 and 1.2 TPa, the highest stress at which a crystal structure has ever been observed. Using angle-dispersive powder x-ray diffraction, we find that dynamically compressed Sn transforms to the body-centered-cubic (bcc) structure previously identified by ambient-temperature quasistatic-compression studies and by zero-kelvin density-functional theory predictions between 0.06 and 0.16 TPa. However, we observe no evidence for the hexagonal close-packed (hcp) phase found by those studies to be stable above 0.16 TPa. Instead, our results are consistent with bcc up to 1.2 TPa. We conjecture that at high temperature bcc is stabilized relative to hcp due to differences in vibrational free energy.

DOI: 10.1103/PhysRevLett.115.075502

PACS numbers: 62.50.-p, 61.05.cp, 64.70.K-

The interplay between the electronic and vibrational contributions to the free energy of a crystal can lead to a rich and complex pressure-temperature phase diagram, especially interesting in regimes where a solid is compressed and heated to the extent that valence electrons are delocalized and standard chemical models for bonding break down. Sn is a particularly fascinating system to explore, because the energetic advantage of sp^3 bonding (which gives the lighter group IV elements their tetrahedral structures) and the energy cost of promoting s electrons to the p band (which drives heavier Pb to take on a face-centered-cubic structure) are nearly balanced. As a result, Sn has several phases which are very close in energy, and their relative stabilities are affected by differences in vibrational and electronic free-energy contributions to the Gibbs free energy at finite temperature. The effects of temperature on phase stability, especially at extreme compression, are not often addressed experimentally or theoretically because of the difficulty of performing these studies (in spite of the fact that in the Universe high pressure is almost always accompanied by temperatures higher than 300 K). Dynamic compression is currently the only experimental method for reaching terapascal stress states (1 TPa = 10×10^6 atmospheres) and elevated temperatures simultaneously. In traditional shock wave experiments, however, the discontinuous rise in entropy results in high-temperature melted states long before terapascal pressures are reached. Shocked Sn reaches the solidus of the melt transition at ~ 0.05 TPa, precluding a study of its solid phases in the terapascal regime. In this work, we use a laser ramp or multishock compression (nanosecond-scale rise time) to probe terapascal states below the melting temperature.

The solid phase diagram of Sn has been explored by using static-compression methods up to 0.2 TPa at 300 K [1] and to 0.1 TPa up to the melting line [2]. In the ground

state, Sn takes on the α (diamond) structure [3] but transforms to the β (tetragonal; β -Sn) structure at 286 K [4]. With increasing pressure, Sn undergoes several more phase transitions: $\beta \rightarrow$ bct (body-centered-tetragonal) \rightarrow bct/bco (body-centered-orthorhombic) mixed phase \rightarrow bcc (body-centered-cubic) \rightarrow hcp (hexagonal-close-packed) [1,5,6]. Theory predicts that, at 0 K, the hcp phase will persist up to ~ 1.3 TPa, after which the bcc phase will again be stabilized [1]. However, at 300 K and 0.22 TPa, the vibrational free energy of the bcc phase is predicted to be slightly lower than that of hcp [7], suggesting that high temperature may also stabilize the bcc phase relative to hcp.

We have succeeded in compressing solid Sn from 0.12 to nearly 1.2 TPa (the highest stress state diffraction measurements yet made) and conclude that the bcc phase is stable over this entire range, including the regime where lower-temperature static measurements find a hcp phase.

The experimental configuration is shown in Fig. 1. Compression is accomplished by ablating a single-crystal $\langle 110 \rangle$ or $\langle 100 \rangle$ -oriented diamond pusher with a temporally shaped laser pulse, creating a rapidly expanding high-energy plasma and generating a compression wave that propagates into the diamond. An 800- μm laser spot size with a super-Gaussian profile is accomplished by using distributed phase plates. The laser intensity is ramped up from 0 to a peak of $0.5 \rightarrow 20 \times 10^{13}$ W/cm² over 3–4 ns and maintained for 1–3 more nanoseconds with the goal of holding a steady stress state in the sample for at least 1 ns. Because of pulse-length limitations and target material response, the Sn drive is likely a multishock rather than a ramp in some of these experiments (Fig. S1 [8]). The compression wave traverses the diamond package, reverberating in the thin Sn and accelerating the rear diamond. The velocity history of the diamond free surface is measured by using velocity interferometry (VISAR)

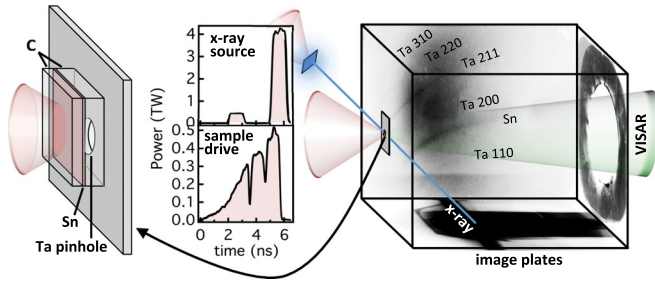


FIG. 1 (color online). Targets consist of $\sim 4\text{-}\mu\text{m}$ Sn foil between single-crystal diamond plates of $\sim 20\text{ }\mu\text{m}$ (pusher) and $\sim 40\text{ }\mu\text{m}$ (tamper), joined by $1\text{--}2\text{-}\mu\text{m}$ layers of epoxy. In some targets, the pusher is formed from two $\sim 15\text{-}\mu\text{m}$ diamond plates sandwiching a $1\text{--}2\text{-}\mu\text{m}$ Au preheat shield. The target is backed by a $300\text{-}\mu\text{m}$ -diameter Ta or Pt pinhole which collimates scattered x rays. The package is mounted on a box lined with image plates. He_α x-ray radiation from a laser-ablated metal foil (incident at 45°) is diffracted off the target, and the Debye-Scherrer rings register as conic sections on the image plates.

[13,14]. Details about the extraction of Sn stress from this velocity history are given in Ref. [15] and Fig. S2. For highest-intensity drives ($> 700\text{ GPa}$), a Au preheat shield between the sample and the ablated diamond is used to prevent preheating and melting of the Sn. At peak compression, x-ray radiation is generated by inducing He_α emission from a $13\text{-}\mu\text{m}$ foil (Fe or Cu) using a 1-ns duration laser pulse (with low-power prepulse to optimize x-ray conversion efficiency [16]). Lasers are defocused to a $300\text{-}\mu\text{m}$ spot without phase plates (peak irradiance on the order of 10^{15} W/cm^2).

Figure 2 shows sample diffraction data at selected stress states over the range in the study, with image plates digitally projected to display constant contours of Bragg angle 2θ , illustrating some of the typical features of these measurements. A spatially broad and smoothly varying background originating from x rays created in the ablation plasma is subtracted from the images by using a nonlinear peak clipping algorithm [17,18]. Some spurious features on the image plates originate from materials positioned in the diagnostic box to absorb x rays from the ablation plasma [such as the strips of plastic evident in Fig. 2(a)] and from the $\text{He-}\beta$ emission [such as the unintentionally wrinkled Cu metal foil evident in Fig. 2(c)]. In rare cases, scattering from another material in the target assembly or diagnostic box is registered on the image plate, as in Fig. 2(b) near $2\theta \sim 93^\circ$. The curvature of this feature indicates that its physical origin is not within the driven sample and has therefore been masked out of the lineout shown in Fig. 2(e). Scattering from the single-crystal diamond windows is sometimes evident: at $2\theta \sim 87^\circ$ in Figs. 2(b) and 2(d) and at $\sim 45^\circ$ in Figs. 2(b)–2(d). The peak is masked out in Fig. 2(d) because it is so intense that the image processing algorithm produces extended artifacts which obscure nearby data [see Fig. S3(b) for the unmasked image]. The position and

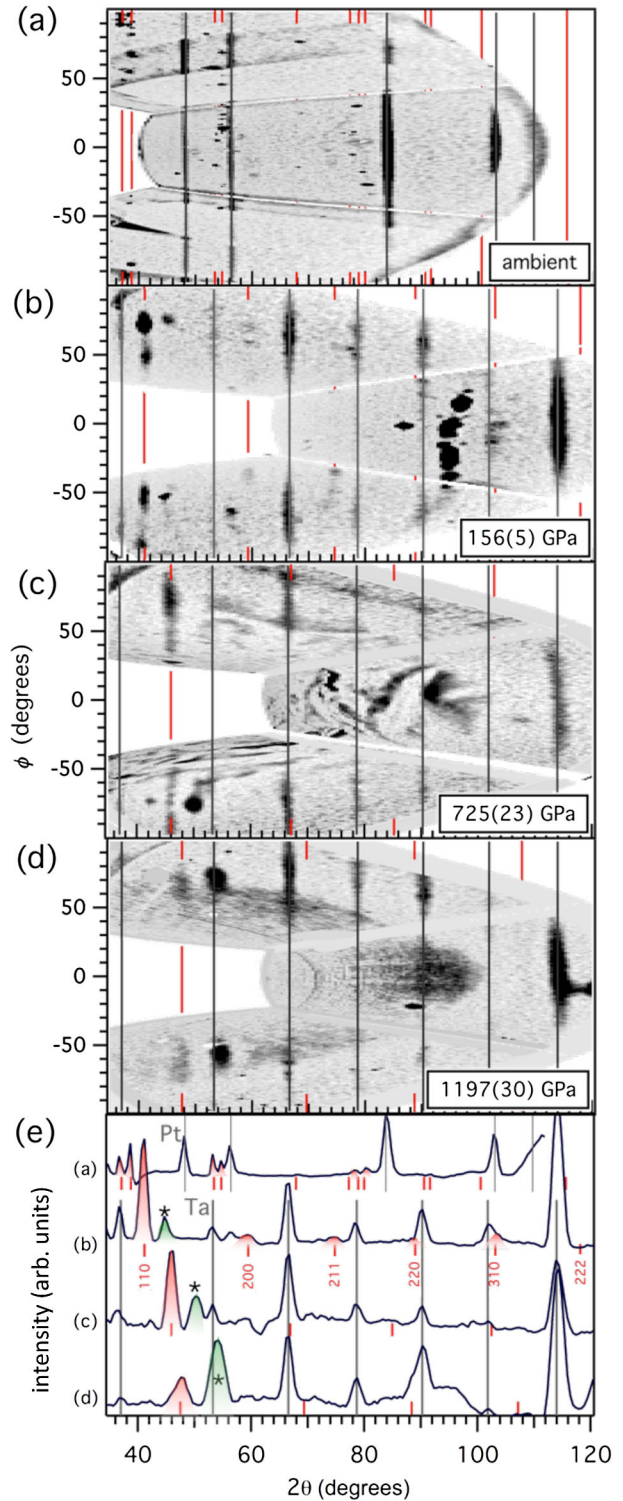


FIG. 2 (color online). X-ray diffraction measurements: (a) Omega EP 13742, (b) Omega 58709, (c) Omega 66028, and (d) Omega 68278. Rectangular image plates are digitally warped to map from detector planes to the azimuthal angle vs Bragg angle. Ideal peak positions for the reference material used for image plate calibration are shown in gray, and Sn ideal peak positions assuming a tetragonal (a) and bcc (b),(c) structure are shown with the red line segments. Suspected diamond peaks are labeled with an asterisk on the image plate lineouts shown in (e).

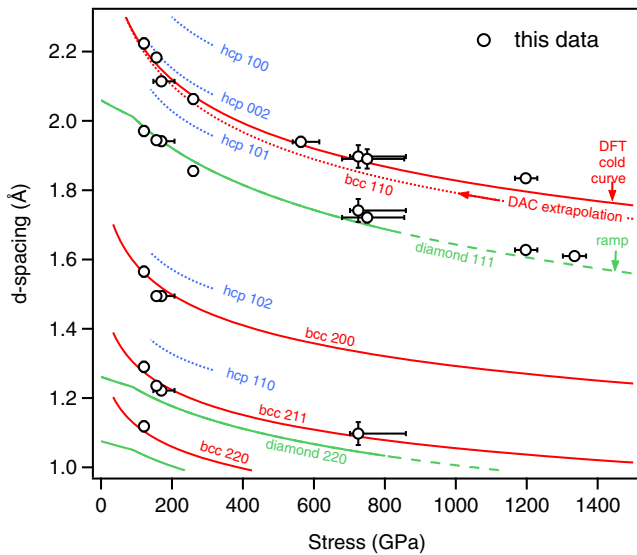


FIG. 3 (color online). d spacing of observed diffraction peaks (data in Table S1), compared with the density-functional theory (DFT) cold curve (red solid line) [1] and with the isothermal equation of state trends and phase transition known from static experiments (dotted lines) [1,5], extrapolated above 180 GPa. The green lines represent the expected trend in diamond d spacing [19] (dashed line, extrapolation above 800 GPa).

character of these peaks are consistent with 111 and 311 reflections from diamond at <80 GPa (further details in Fig. S3). The strong, continuous diffraction peaks marked with gray lines in Figs. 2(a)–2(d) are from the ambient-pressure pinhole material [platinum in Fig. 2(a) and tantalum in Figs. 2(b)–2(d)], which are used for angular calibration of the image plates.

Diffraction from ambient Sn (99.9% purity Goodfellow rolled foil) shown in Fig. 2(a) is sparse and spotty, indicating that the foils have large, randomly distributed crystallites. The ambient Sn data are consistent with the expected β -Sn structure, although there is some ($<1\%$) deviation from ideal peak position, due to poor statistical sampling of large, mildly strained crystallites.

From 120 to 170 GPa [Fig. 2(b)], Sn is in the bcc phase, consistent with the static-compression measurements of the bcc phase up to at least 180 GPa [1]. The phase transition to bcc caused a significant change in the microstructure compared to the ambient scattering. The intensity variation as a function of the azimuthal angle indicates preferred orientation of crystallites, but the distribution in ϕ and the smoothness of the peaks indicate decreased grain sizes. The stress-induced shifts in the peak positions agree well with the ideal shifts in d spacing with stress for all peaks (Fig. 3 and Table S1), indicating that the cubic crystal structure is not significantly distorted under the strong uniaxial loading.

Above 200 GPa, we observe only 1–3 diffraction peaks, and their positions are not consistent with the transition to hcp observed in static measurements (Fig. 3). While this

number of peaks is insufficient to uniquely identify a crystal structure, we narrow the range of possibilities by considering the density that the peak positions imply (density drops or large density jumps upon stress increase are considered unlikely) and the probability of observing the registered peak, based on the expected peak intensities for the hypothesized crystal symmetry. If we assume that there must be a transition to an hcp structure near 200 GPa (a martensitic transition and therefore likely to take place at these time scales [20]) and assign our two dominant peaks as the hcp 100 and 101 reflections, we find an unreasonably large density jump of $\sim 11\%$ (Fig. S4). An assignment of the higher d -spacing peak as the 002 peak from the hcp phase produces a smoother density trend but is unlikely, based on the expectation that the 100 and 101 peak intensities should be greater for hcp symmetry. Unusual peak intensity ratios could occur if there is a strong preferred orientation in the sample as a result of anisotropic response, but the 002 peak should not, in that case, be the most intense for this geometry [21]. The hexagonal ω phase, although not predicted to be stable for Sn, is another martensitic transition commonly observed in close-packed metallic systems [22], but a treatment of the two intense peaks as the 110 and 101 ω reflections would also require an 11%–12% density jump.

The position and shift of the higher d -spacing peak are consistent with an extrapolation of the Sn bcc 110 peak shift [1], and the lower d -spacing peak is consistent with the expected diamond peak shift [19]. This latter peak [labeled with an asterisk in Fig. 2(e)] is azimuthally localized but more extended than the single-crystal diamond reflections, suggesting that the single crystals fragment upon compression and the crystallites adopt a distinct preferred orientation. This unusual behavior has not been positively verified, and further studies to understand the nature of single-crystal diamond at extreme dynamic compression are underway. Based on the peak positions, however, we conclude that the most reasonable interpretation of these results is that Sn remains in the bcc phase; we do not see the hcp phase transition observed in static measurements; and the textured diffraction feature at lower d spacing originates from diamond. Given the lack of texture and the relatively high signal to background (~ 0.45) of the Sn peak, and assuming the structure is indeed bcc, several higher angle peaks would be expected to be observable above the background. This lack of intensity in the higher angle peaks suggests a large mean-square displacement and a small Debye-Waller factor, consistent with temperatures in the thousands of kelvins. However, a reliable evaluation of the Debye-Waller factor to estimate temperature requires an accurate account of lattice anharmonicity and volume dependence of the Debye temperature, which is beyond the scope of this Letter.

Above 1 TPa, the Sn peak has broadened and weakened compared to lower-stress measurements, possibly indicating more significant heating or closer proximity to melt,

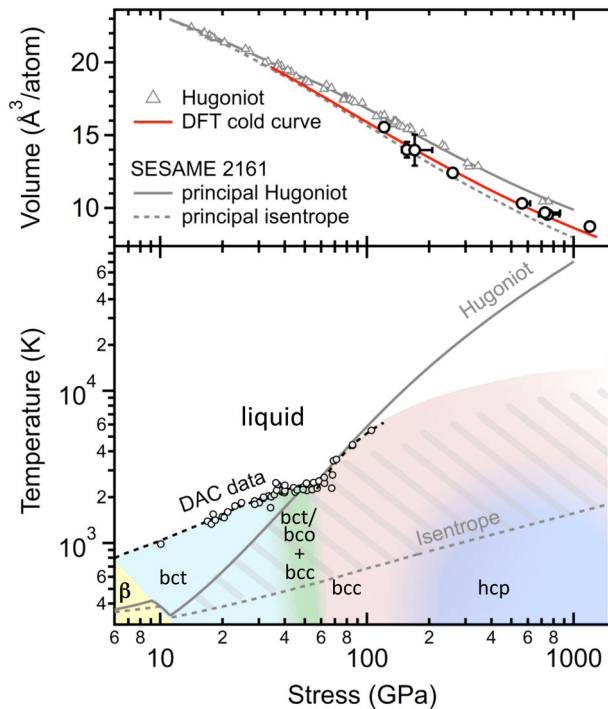


FIG. 4 (color online). Top: Equation of state of Sn, assuming a bcc phase, compared to the DFT cold curve [1], Hugoniot data [26], and tabulated equation of state model SESAME 2161 [23]. Bottom: Phase diagram of Sn known from static and shock studies [1,2,27–29]. The thermodynamic path followed in this study is unknown, but the temperature is bounded by the gray hashed region.

since it can be correlated with the formation of a strong shock in the velocity history at the rear diamond surface of the target [Fig. S3(b)]. Because dynamically compressed diamond loses transparency beyond the elastic limit due to fracture, it is impossible to determine precisely where the shock formed within the sample, but it is possible that Sn is more strongly heated. One shot at 1.33 TPa which also displayed a strong shock at the diamond free surface had no distinguishable diffraction from Sn (Fig. S3), suggesting that at these conditions the sample may have melted entirely.

The experimental equation of state of Sn is shown in Fig. 4, assuming that the bcc structure is maintained over the entire stress range. The compressibility falls between the SESAME 2161 principal isentrope and Hugoniot [23]. The lower panel of Fig. 4 illustrates the current understanding of the Sn phase diagram and the region of phase space which our results inform. All previous measurements and theoretical predictions of the hcp phase have been made between 0 and 300 K. The thermodynamic path for ramp-compressed materials is bounded at lower temperature by the principal isentrope and at upper temperature by the second-shock Hugoniot from an initial shock to ~ 70 GPa (which represents the strength of the diamond elastic shock transmitted into Sn [24]). Accurate

methods for measuring temperature remain an important challenge. Temperature estimates for a multishock path based on EXAFS measurements have been made for iron [25], showing that the temperature falls roughly midway between the isentrope and the Hugoniot.

There are at least two possible explanations for the different dynamic- and static-compression phase observations: the hcp phase may not be the energetically stable phase at the high temperatures in our experiment, or the strain rates in our experiment may be too rapid for nucleation and growth of the hcp phase to be observed. The activation free-energy barrier to formation of the hcp phase in the Sn system (and the effect of pressure on that barrier) has not been reported, so we cannot rule out the possibility of a kinetically hindered transition. However, metadynamics simulations at 200 GPa and 300 K find that the transition is initiated in the very first time step, indicating a very low free-energy barrier to formation of hcp [7].

The presence of a high-temperature bcc phase stabilized over hcp (or similarly close-packed fcc) is in fact common for elemental metals across the periodic table (including electronically similar Pb [30]) and the mechanism extensively discussed [31–35]. The bcc structures generally have softer phonons (slightly lower Debye temperature) than the close-packed phases, giving them higher vibrational entropy. They also tend to have a higher density of electronic states at the Fermi level and, thus, higher electronic entropy. The higher total entropy in the bcc phase will diminish the free-energy difference between the two phases at high temperature [36,37]. When anharmonicity is taken into account, the stability of bcc relative to hcp is even higher. In many cases, when hcp is the stable ground state phase and bcc is observed experimentally at high temperature, theoretical calculations significantly overestimate the transition temperature unless the anharmonicity is accurately modeled. This demonstrates that anharmonic phonon contributions to the free energy at high temperature play an important role in counterbalancing the lower enthalpy of the hcp phase [35].

The ground state free-energy difference between the bcc and hcp phases in Sn is very small (< 40 meV/atom over the entire pressure range where hcp is stable [1,7]). Even within the harmonic approximation, by 300 K the vibrational free energy of bcc is already predicted to be slightly lower than that of hcp [7]. It is likely that, should anharmonic effects be taken into account and first-principles calculations extended to thousands of kelvins, bcc will be stabilized relative to hcp for Sn.

In summary, we have performed x-ray diffraction measurements from 0.12 to 1.2 TPa, which is the highest stress state at which crystal structure has ever been directly probed. Our results suggest that the bcc phase is stable over this entire range, in contrast to quasistatic loading experiments at room temperature which find an hcp phase. Kinetic effects may play a role in suppressing the transition to hcp, but it is also plausible that bcc is stabilized below

the melting curve by differences in vibrational free energy which could compensate for the lower ground state enthalpy of the hcp phase. These results demonstrate that temperature can play a significant role in stabilizing unpredicted phases at extreme conditions and emphasize the importance of considering finite temperatures in structure prediction and for developing methods for accurately measuring temperature.

We acknowledge helpful discussions with P. F. McMillan, D. Klug, Y. Yao, L. Burakovsky, A. Salamat, and C. Pickard, target fabrication by S. Uhlich, W. Unites, and T. Uphaus, and support at the Laboratory for Laser Energetics by C. Sorce, N. Whiting, and J. Tellinghuisen. This work was performed under the auspices of the U.S. Department of Energy by Lawrence Livermore National Laboratory under Contract No. DE-AC52-07NA27344.

-
- [1] A. Salamat, G. Garbarino, A. Dewaele, P. Bouvier, S. Petitgirard, C. J. Pickard, P. F. McMillan, and M. Mezouar, *Phys. Rev. B* **84**, 140104(R) (2011).
- [2] R. Briggs, D. Daisenberger, A. Salamat, G. Garbarino, M. Mezouar, M. Wilson, and P. F. McMillan, *J. Phys. Conf. Ser.* **377**, 012035 (2012).
- [3] A. Jayaraman, *Rev. Mod. Phys.* **55**, 65 (1983).
- [4] J. D. Barnett, V. E. Dean, and H. T. Hall, *J. Appl. Phys.* **37**, 875 (1966).
- [5] S. Desgreniers, Y. K. Vohra, and A. L. Ruoff, *Phys. Rev. B* **39**, 10359 (1989).
- [6] A. Salamat, R. Briggs, P. Bouvier, S. Petitgirard, A. Dewaele, M. E. Cutler, F. Corà, D. Daisenberger, G. Garbarino, and P. F. McMillan, *Phys. Rev. B* **88**, 104104 (2013).
- [7] Y. Yao and D. Klug, *Solid State Commun.* **151**, 1873 (2011).
- [8] See Supplemental Material at <http://link.aps.org/supplemental/10.1103/PhysRevLett.115.075502> for description of pressure determination, a more detailed summary of the data presented in this paper, and a discussion of the extraneous diffraction signatures from single crystal diamond evident for some of the shots included in this paper, which includes Refs. [9–12].
- [9] D. E. Fratanduono, T. R. Boehly, P. M. Celliers, M. A. Barrios, J. H. Eggert, R. F. Smith, D. G. Hicks, G. W. Collins, and D. D. Meyerhofer, *J. Appl. Phys.* **110**, 073110 (2011).
- [10] S. Brygoo, E. Henry, P. Loubeyre, J. Eggert, M. Koenig, B. Loupias, A. Benuzzi-Mounaix, and M. R. Le Gloahec, *Nat. Mater.* **6**, 274 (2007).
- [11] J. H. Eggert, D. G. Hicks, P. M. Celliers, D. K. Bradley, R. S. McWilliams, R. Jeanloz, J. E. Miller, T. R. Boehly, and G. W. Collins, *Nat. Phys.* **6**, 40 (2010).
- [12] M. D. Knudson, M. P. Desjarlais, and D. H. Dolan, *Science* **322**, 1822 (2008).
- [13] L. M. Barker and R. E. Hollenbach, *J. Appl. Phys.* **43**, 4669 (1972).
- [14] P. M. Celliers, D. K. Bradley, G. W. Collins, D. G. Hicks, T. R. Boehly, and W. J. Armstrong, *Rev. Sci. Instrum.* **75**, 4916 (2004).
- [15] J. R. Rygg *et al.*, *Rev. Sci. Instrum.* **83**, 113904 (2012).
- [16] D. Babonneau *et al.*, *Phys. Plasmas* **15**, 092702 (2008).
- [17] C. G. Ryan, E. Clayton, W. L. Griffin, S. H. Sie, and D. R. Cousens, *Nucl. Instrum. Methods Phys. Res., Sect. B* **34**, 396 (1988).
- [18] M. Morháč, J. Kliman, V. Matoušek, M. Veselský, and I. Turzo, *Nucl. Instrum. Methods Phys. Res., Sect. A* **401**, 113 (1997).
- [19] D. K. Bradley, J. H. Eggert, R. F. Smith, S. T. Prisbrey, D. G. Hicks, D. G. Braun, J. Biener, A. V. Hamza, R. E. Rudd, and G. W. Collins, *Phys. Rev. Lett.* **102**, 075503 (2009).
- [20] N. V. Chandra Shekar and K. Govinda Rajan, *Bull. Mater. Sci.* **24**, 1 (2001).
- [21] H.-R. Wenk, S. Matthies, R. J. Hemley, H.-K. Mao, and J. Shu, *Nature (London)* **405**, 1044 (2000).
- [22] S. K. Sikka, Y. K. Vohra, and R. Chidambaram, *Prog. Mater. Sci.* **27**, 245 (1982).
- [23] C. Greeff *et al.*, Report No. LA-UR-05-9414, 2005.
- [24] R. S. McWilliams, J. H. Eggert, D. G. Hicks, D. K. Bradley, P. M. Celliers, D. K. Spaulding, T. R. Boehly, G. W. Collins, and R. Jeanloz, *Phys. Rev. B* **81**, 014111 (2010).
- [25] Y. Ping *et al.*, *Phys. Rev. Lett.* **111**, 065501 (2013).
- [26] Russian shock wave database, <http://teos.ficp.ac.ru/rusbank/>.
- [27] B. Schwager, M. Ross, S. Japel and R. Boehler, *J. Chem. Phys.* **133**, 084501 (2010).
- [28] P. L. Hereil and C. Mabire, *J. Phys. IV (France)* **10**, Pr9-799 (2000).
- [29] J. Hu, X. Zhou, C. Dai, H. Tan, and J. Li, *J. Appl. Phys.* **104**, 083520 (2008).
- [30] A. Dewaele, M. Mezouar, N. Guignot, and P. Loubeyre, *Phys. Rev. B* **76**, 144106 (2007).
- [31] S. Alexander and J. McTague, *Phys. Rev. Lett.* **41**, 702 (1978).
- [32] J. Friedel, *J. Phys. Lett. (Paris)* **35**, 159 (1974).
- [33] R. E. Watson and M. Weinert, *Phys. Rev. B* **30**, 1641 (1984).
- [34] G. Grimvall, B. Magyari-Köpe, V. Ozoliņš, and K. A. Persson, *Rev. Mod. Phys.* **84**, 945 (2012).
- [35] P. Souvatzis, O. Eriksson, M. I. Katsnelson, and S. P. Rudin, *Phys. Rev. Lett.* **100**, 095901 (2008).
- [36] E. G. Moroni, G. Grimvall, and T. Jarlborg, *Phys. Rev. Lett.* **76**, 2758 (1996).
- [37] S. R. Nishitani, H. Kawabe, and M. Aoki, *Mater. Sci. Eng. A* **312**, 77 (2001).